Length and time scales for precipitation during carbon mineralization

M.A. Chen[1], W. Yang[1], H. Peng[1], P.K. Kang[1,2], and V.R. Voller[3,2,*]

[1]Department of Earth and Environmental Sciences, University of Minnesota, Minneapolis, MN, 55455, USA
[2]St. Anthony Falls Laboratory, University of Minnesota, Minneapolis, MN 55455, USA
[3]Department of Civil, Environmental, and Geo- Engineering, University of Minnesota, Minneapolis, MN, 55455
[*]Corresponding author

January 9, 2024

Key points

- We develop a first-order carbon mineralization model and perform a scaling analysis to identify key length and time scales

- Through the scaling analysis, we define expressions for the operational length and shutoff time of a mineralization operation

- Using typical field data we estimate a range of shutoff times and an effective first-order precipitation rate constant

Abstract

In this study, we identify the key length and time scales associated with CO_2 mineralization in basalt reservoirs. This is achieved through the development and application of a simple yet complete model of the fate and transport of a supersaturated CO_2-charged fluid moving unidirectionally through an initially uniform basalt rock. The model consists of three coupled equations describing, (i) the spatiotemporal evolution of porosity with the mineralization reaction, (ii) the resulting temporal and spatially varying fluid discharge, and (iii) the fate and transport of the mineralization reactant(s) in the aqueous phase. A dimensional analysis provides length and time scales that characterize the extent and duration of field-scale carbon mineralization. These scales are applied to a field site to estimate poorly constrained mineralization parameters, notably, the effective first-order reaction rate constant.

Plain Language Summary

A promising method to combat global climate change is to sequester carbon dioxide through carbon mineralization. Unlike geologic carbon sequestration, where carbon must remain trapped in aquifers for millennia by an intact caprock, carbon mineralization securely stores carbon by rapidly converting injected carbon dioxide into carbonate rocks. A major challenge in designing these systems, however, is knowing how aquifer properties and injection parameters determine how large a mineralization site must be as well as the time over which it can operate before clogging. Here, we develop a simple model based on the formation of carbonate rocks in a basalt aquifer and analyze it to determine these necessary length and time scales. We find that the length scale of mineralization depends on the injection pressure, aquifer conductivity, and reaction rate of carbonation, while the time scale for shutoff depends on initial porosity, reaction rate, and

how efficiently the carbonate minerals can fill the aquifer. We also show, using typical carbon mineralization field data, how this scaling can be used to estimate a range of values for an effective reaction rate constant. Together, the modeling and scaling results provide powerful tools for the research and development of carbon mineralization.

1   Introduction

Carbon sequestration technologies have long been considered a primary pathway of mitigating climate change arising from the overabundance of CO_2 gas in our atmosphere. An emerging technology that shows promise is the capture of carbon in the subsurface through the mineralization of CO_2 by injection into mafic (basalts) and ultramafic rock reservoirs [Snæbjörnsdóttir et al., 2017, 2018, 2020, Clark et al., 2020, Kelemen et al., 2020, Power et al., 2013, Matter et al., 2016, White et al., 2020]. The advantage of this approach is that it 'locks' the carbon into the rock, handily mitigating the risk of CO_2 leaking back into the atmosphere. Conventional approaches (i.e. through geologic storage) in relatively inert aquifers predict mineralization occurs, but only after tens of thousands of years. By contrast, aquifers containing mafic and ultramafic rocks can be dissolved by CO_2, liberating cations that result in precipitation of carbonate rocks in a matter of only a few years. The starting point for engineering carbon mineralization is to identify the factors that enhance or limit the ability to precipitate carbonate minerals in subsurface rock masses. This is the first step toward ultimately answering the critical questions: *For a given mineralization process what is the ultimate capacity of carbon that can be stored?* and *How long will it take for this capacity to be realized?*

In determining the potential storage of a given aquifer there are two end members. At one end we might consider using reservoirs of ultramafic rock (e.g., peridotite) which are highly reactive to carbon mineralization but have very low permeability. Here, the capacity of the operation will rest on engineering fluid flow by creating and maintaining fluid flow paths [Kelemen et al., 2020]. This could be accomplished by leveraging the mechanical forces unleashed by the expanding mineralization products, known as reaction driven cracking. At the other end, we might use basalt reservoirs (as in the CarbFix project in Iceland or Wallula Basalt Pilot Project in the United States) where mineralization reactions are slower, but permeabilities are large enough to permit flow [Snæbjörnsdóttir et al., 2018, Callow et al., 2018, Snæbjörnsdóttir et al., 2020, Matter et al., 2016, White et al., 2020]. In this case, which will be our focus here, determining the carbon storage potential essentially reduces to estimating the length and time scales of a field operation, in particular:

1. *The process length scale (i.e. aquifer size) needed to achieve complete mineralization of carbon from an injected CO_2 laden fluid*

2. *The process time before the precipitate products 'clog' and terminate flow pathways*

Our methodology to make these estimates will be through the development of a model that describes the interacting coupled chemical and transport processes that are involved, focused on a case where precipitation is the rate limiting process compared to dissolution. By applying a dimensional scaling analysis to the model, we identify and extract the relevant length and time scales that control carbon mineralization. We demonstrate that these length and time scales provide critical and fundamental information for designing successful carbon mineralization processes in basalt and similar rock masses.

2   A Carbon Mineralization Precipitation Model

2.1   Overview of Model

Towards the aim of determining the carbon mineralization storage potential of a given reservoir, we will consider a model system where a prescribed constant pressure head gradient transports CO_2-charged water through a one-dimensional porous reservoir of length $0 \leq x \leq L$, see Fig. 1. We consider simplified precipitation reaction cases, such as $A(aq) + B(aq) \rightarrow P(s)$, where an injected reactant A mixes with reactant B in the aquifer to form a precipitate. In the case of carbon mineralization in mafic or ultramafic rocks, A, B, and P might represent carbonate ions, cations released by the dissolved host rocks, and precipitated carbonate minerals, respectively. As the precipitate forms it will decrease the porosity in the reservoir, which

in turn decreases the flow, eventually leading to complete clogging of the reservoir and a flow shutoff. The overall aim of the model is to identify the length over which mineralization occurs before shutoff terminates the operation. This requires construction of three interacting and coupled model components:

1. an expression for the porosity change within the pore spaces as a function of mineral precipitation on the pore surfaces, which is driven by the reaction of dissolved carbonate and cations,

2. an equation to describe the flow of the fluid through the reservoir, accounting for changes of porosity in space, and

3. an equation describing the fate and transport of the aqueous mineralization reaction reactants, also accounting for changes in porosity in space.

In total these components are able to describe and account for the competition between the flow of the CO_2-charged water and the clogging of the flow pathways.
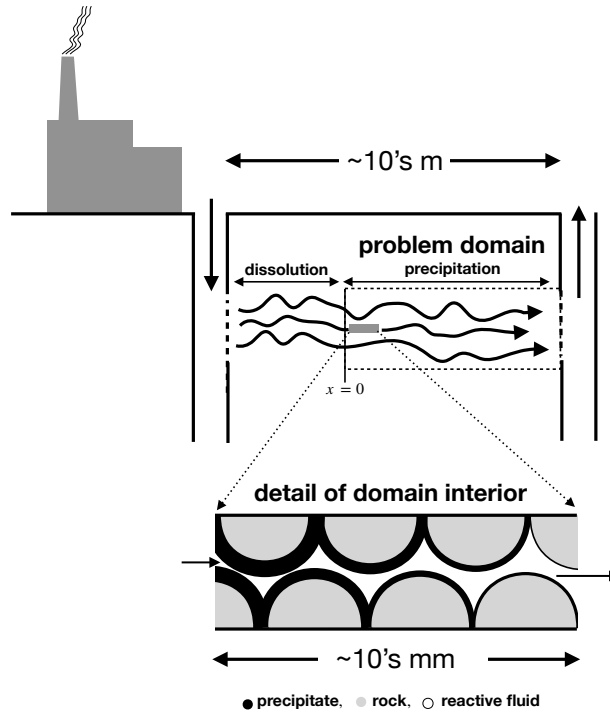

Figure 1: Schematic of a carbon mineralization operation and a representation of the problem domain whose entrance is where precipitation initiates, $x = 0$, and whose exit is at the outflow at $x = L$. This is the porous media reservoir over which precipitation occurs. The model describes the system at the continuum scale, but the schematic provides a view of the pore scale for reference to how precipitation and pore clogging is effectively modeled.

2.2   Key Assumptions

Before we begin to derive our governing equations and relationships, we emphasize that the objective in building our model is to balance between simplicity and reality. We aim to capture the first-order critical features of the system, simplifications that will provide identification of the key process and phenomena controlling the length and time scales. In this light, the key assumptions in our model are the following:

1. We only consider precipitation in the domain of interest, i.e., dissolution reactions, dissolving the host rock and releasing cations for mineralization, occur upstream of the domain entrance at $x = 0$.

2. The sole reaction that forms the mineral precipitate has unit stoichiometry with pseudo-first-order kinetics.

3. Precipitation occurs only on pore surfaces.

4. To leading order, as precipitation occurs, the hydraulic conductivity and specific surface area are functions of the porosity, i.e.,

$$K(x,t) = K_i g_k(\phi(x,t)) \tag{1}$$

and

$$S(x,t) = S_i g_s(\phi(x,t)), \tag{2}$$

where K_i [m/s] and S_i [m^2/m^3] are the values of the conductivity and specific surface area at the initial porosity, ϕ_i, and the values of the functions at the initial porosity are $g_k(\phi_i) = g_s(\phi_i) = 1$.

5. The flow through the porous medium is governed by Darcy's law, i.e., the discharge q [m^3/m^2/s] (volume flux per unit cross-sectional area of the porous medium), is given by

$$q(x,t) = \phi u(x,t) = -K(x,t)\frac{\partial h}{\partial x} = -K_i g_k(\phi)\frac{\partial h}{\partial x} \tag{3}$$

where $u(x,t)$ [m/s] is the seepage velocity (the fluid velocity in the pore spaces) and $h(x,t)$ [m] is the pressure head.

6. At the initial time, before the reactants are introduced, the porosity ϕ, hydraulic conductivity K [m/s], and specific surface area S [m^2/m^3] of the porous medium in the domain take constant values.

7. The fluid density and precipitate densities in the porous medium take constant values where changes in density due to chemical reactions or the dissolution of CO_2 into pore fluids are assumed to be negligible.

2.3 Model Components

2.3.1 Precipitation Reaction

As stated, the rate law for the precipitation reaction is assumed to be pseudo first-order in the reactant concentration C,

$$r = k^* S_i g_s(\phi) \left(1 - \frac{C}{C_{eq}}\right) = k g_s(\phi)(C_{eq} - C) \tag{4}$$

where k^* is the geochemical reaction rate constant [mol/m^2/s], C_{eq} the equilibrium concentration of the main reactants [mol/m^3], and $k = k^* S_i/C_{eq}$ is the pseudo-first-order reaction rate constant. The use of pseudo first-order rate laws is a common practice in the interpretation and modeling of precipitation reactions [Morse et al., 2007, Nancollas and Reddy, 1971, Reddy and Nancollas, 1971, 1976, Lasaga, 1997]. A geochemical derivation of this expression from transition state theory, as well as special cases where these first-order kinetics will readily appear is discussed in the Supporting Information.

2.3.2 The Porosity Change

The reaction rate in eq. (4) represents the rate at which reactant is consumed per unit volume of the domain. This rate of consumption will be related in the rate of formation of new solid volume per unit volume of the domain through precipitation, expressed as the negative rate of the change of porosity $-\frac{\partial \phi}{\partial t}$. Noting our unit stoichiometry, reactant mass conservation (i.e. mass of reactant plus the precipitate) gives the relation between consumption of reactant and rate of increase of volume by the precipitate as

$$\frac{\partial \phi}{\partial t} = \nu_S r = \nu_S k g_s(\phi)(C_{eq} - C) \tag{5}$$

where ν_S is the molar volume of the precipitate; the appropriate initial condition for this rate equation is $\phi(x,0) = \phi_i$.

2.3.3 Flow

Due to our assumptions of constant, but potentially different densities in the liquid and solid phases, the rate of change in mass, in a fixed control volume, due to the formation of precipitates is

$$\dot{m} = (\rho - \rho_p)\frac{\partial \phi}{\partial t}, \tag{6}$$

$\rho \; [\mathrm{kg/m^3}]$ is the liquid density and $\rho_p \; [\mathrm{kg/m^3}]$ is the density of the precipitate. This mass rate is related to the net rate of flow in and out of the volume, which can be expressed in terms of the divergence of the discharge, i.e.,

$$\dot{m} = (\rho - \rho_p)\frac{\partial \phi}{\partial t} = -\rho\frac{\partial q}{\partial x} \tag{7}$$

On dividing through by the fluid density ρ, defining the density ratio $\rho_r = \rho_p/\rho$, and using both Darcy's law [eq.(3)] and the expression for porosity change [eq.(5)], we can write this balance as the following equation,

$$(1 - \rho_r)\nu_S k g_s(\phi)(C_{eq} - C) = \frac{\partial}{\partial x}\left([K_i g_k(\phi)]\frac{\partial h}{\partial x}\right), \quad 0 \leq x \leq L, \tag{8}$$

with initial condition $\phi(x,0) = \phi_i$ and boundary conditions of prescribed heads at the ends of the domain, i.e., $h(0,t) = h_0 > h(L,t) = h_L$.

2.3.4 Reactant Fate and Transport

We also require an advection-dispersion-reaction model to describe the fate and transport of the reactant, given by

$$\begin{aligned}
\frac{\partial (\phi C)}{\partial t} =& \frac{\partial}{\partial x}\left([K_i g_k(\phi)]\frac{\partial h}{\partial x}C\right) + \frac{\partial}{\partial x}\left(D\frac{\partial C}{\partial x}\right) \\
&+ k g_s(\phi)(C_{eq} - C) + \frac{\partial \phi}{\partial t}C, \quad 0 \leq x \leq L,
\end{aligned} \tag{9}$$

with initial condition $C(x,0) = C_{eq}$ as well as boundary conditions $C(0,t) = C_0$, and $(\partial C(L,t)/\partial x) = 0$. The first term on the right-hand side of eq.(9) is the contribution from advective transport. The second term accounts for the contribution of dispersive transport, where $D = D_L + \phi D_m$ is the dispersion coefficient $[\mathrm{m^2/s}]$; D_L is the longitudinal dispersion and D_m is the molecular diffusion. The third term is the rate of consumption of the reactant in forming the precipitate, see eq.(4). The last term accounts for the loss of fluid mass due to precipitation reducing the pore space. On combining this last term with the left-hand side, we can rewrite the fate and transport equation as

$$\begin{aligned}
\phi\frac{\partial C}{\partial t} =& \frac{\partial}{\partial x}\left(K_i g_k(\phi)\frac{\partial h}{\partial x}C\right) + \frac{\partial}{\partial x}\left(D\frac{\partial C}{\partial x}\right) \\
&+ k g_s(\phi)(C_{eq} - C), \quad 0 \leq x \leq L,
\end{aligned} \tag{10}$$

In further developing this model we will neglect contributions from molecular diffusion because we should expect this to be orders of magnitude smaller than the longitudinal dispersion. Thus, following Bear [1972], we can model the dispersion coefficient as

$$D = D_L = \alpha_L u = \alpha_L \left(\frac{q}{\phi} \right) \tag{11}$$

where α_L [m] is the longitudinal dispersivity. Typically, α_L scales with the domain size as shown in Gelhar et al. [1992], i.e, $\alpha_L = \beta_L L$, a choice that, on using the Darcy expression for discharge [eq. (3)] and the expression for g_k, generates the following model for the dispersion coefficient,

$$D = -\beta_L L \frac{K_i g_k(\phi)}{\phi} \frac{\partial h}{\partial x}, \tag{12}$$

which assumes that the head gradient is negative. On inserting this treatment into our fate and transport model [eq. (9)], we arrive at the advection-dispersion-reaction equation

$$\phi \frac{\partial C}{\partial t} = \frac{\partial}{\partial x} \left(K_i g_k(\phi) \frac{\partial h}{\partial x} C - \beta_L L \left[\frac{K_i g_k(\phi)}{\phi} \frac{\partial h}{\partial x} \right] \frac{\partial C}{\partial x} \right) + \\ k g_s(\phi)(C_{eq} - C), \quad 0 \le x \le L. \tag{13}$$

2.4 A Model of Carbon Mineralization

Gathering the appropriate equations together, the coupled model for carbon mineralization through precipitation is formed as:

Porosity [eq. (5)] :

$$\frac{\partial \phi}{\partial t} = \nu_S k g_s(\phi)(C_{eq} - C),$$

with $\phi(x, 0) = \phi_i$.

Flow [eq. (8)]:

$$(1 - \rho_r)\nu_S k g_s(\phi)(C_{eq} - C) = \frac{\partial}{\partial x} \left(K_i g_k(\phi) \frac{\partial h}{\partial x} \right), \quad 0 \le x \le L,$$

with $\phi(x, 0) = \phi_i$, $h(0, t) = h_0$, and $h(L, t) = h_L$.

Reactant fate and transport [eq. (13)]:

$$\phi \frac{\partial C}{\partial t} = \frac{\partial}{\partial x} \left(K_i g_k(\phi) \frac{\partial h}{\partial x} C - \beta_L L \left[\frac{K_i g_k(\phi)}{\phi} \frac{\partial h}{\partial x} \right] \frac{\partial C}{\partial x} \right) + \\ k g_s(\phi)(C_{eq} - C), \quad 0 \le x \le L,$$

with $C(x, 0) = C_{eq}$, $C(0, t) = C_0$, and $(\partial C(L, t)/\partial x) = 0$.

2.5 Examples of Constitutive Models

As noted, to solve the coupled model equations [eqs. (5), (8), (13)], we will need to introduce constitutive models for the hydraulic conductivity and specific surface area functions, $g_k(\phi)$ and $g_s(\phi)$, respectively. Here, fully recognizing the existence of alternative choices, we provide a basic example of a constitutive model for each of these variables.

2.5.1 Hydraulic Conductivity

A classical model for the hydraulic conductivity would be Kozeny-Carman, though other models can be used as appropriate [Kozeny, 1927, Sabo and Beckingham, 2021, Carman, 1997]. This would set the conductivity function g_k as

$$g_k(\phi) = \frac{\phi^3 (1 - \phi_i)^2}{(1 - \phi)^2 \phi_i^3} \tag{14}$$

6

2.5.2   Specific Surface Area

Experiments and measurements indicate that it is reasonable to expect that specific surface will trend upwards with decreasing porosity [Noiriel et al., 2009, Helgeson et al., 1984]. A general representation of this behavior can be captured by setting the specific surface area as

$$g_s(\phi) = \frac{(1-\phi)^m}{(1-\phi_i)^m}$$
(15)

where $m \geq 0$. Here, to explore the range of possibilities, we will consider two end-members. Setting $m = 1$ results in a linear increase in specific surface area with decreasing porosity, while setting $m = 0$ makes the specific surface area constant with respect to porosity.

3   Dimensional Analysis

For a given domain length L and specified constitutive models for hydraulic conductivity and specific surface area, the solution of the governing equations in section 2.4 requires specifying 10 parameters

$$[k, \nu_S, C_{eq}, C_0, K_i, \rho_r, h_0, h_L, \beta_L, \phi_i],$$

some of which may be difficult to fully characterize. Below we carry out a dimensional analysis to reduce the number of parameters. This is done in two steps. First through developing a non-dimensional form of the governing equations, followed by a scaling analysis that eliminates lower order terms.

3.1   Dimensionless Model Equations

We propose the following dimensionless scalings for space, time, pressure head, and reactant concentration

$$\xi = \sqrt{\frac{k}{K_i \Delta h}} x, \quad \tau = \nu_S(C_0 - C_{eq})kt, \quad \eta = \frac{h - h_L}{\Delta h}, \quad \Gamma = \frac{C - C_{eq}}{C_0 - C_{eq}}.$$
(16)

The choice of length scale captures the competing effects of advective transport and reaction on the reactant concentration. We can expect that in cases where reaction is very fast compared to transport that the resulting profiles of flow and concentration will be compressed, and vice versa, with slow reaction and fast flow stretching concentration profiles out. The choice of time scale normalizes time to the initial rate of porosity formation.

With these scalings in hand we can define the following dimensionless parameters: the dimensionless domain length

$$\ell = \sqrt{\frac{k}{K_i \Delta h}} L,$$
(17)

the dimensionless flow discharge (Darcy Flux)

$$\psi = -g_k(\phi)\frac{\partial \eta}{\partial \xi},$$
(18)

the yield (the relative volume of the precipitate created by the reaction)

$$Y = \nu_S C_0,$$
(19)

and the initial supersaturation ratio

$$R = \frac{C_0}{C_{eq}}.$$
(20)

Further, on making the substitutions

$$x = \sqrt{\frac{K_i \Delta h}{k}} \xi, \quad t = \frac{\tau}{\nu_S k(C_0 - C_{eq})}, \quad h = \eta \Delta h + h_L,$$

$$C = \Gamma(C_0 - C_{eq}) + C_{eq}, \tag{21}$$

into eqs. (5), (8), and (13), we arrive at the following set of dimensionless equations:

Porosity:

$$\frac{\partial \phi}{\partial \tau} = -g_s(\phi)\Gamma \tag{22}$$

with $\phi(\xi, 0) = \phi_i$.

Flow:

$$-(1 - \rho_r)Y \left(1 - \frac{1}{R}\right) g_s(\phi)\Gamma = \frac{\partial}{\partial \xi}\left(g_k(\phi)\frac{\partial \eta}{\partial \xi}\right) = -\frac{\partial \psi}{\partial \xi} \tag{23}$$

with $\eta(0, \tau) = 1$ and $\eta(\ell, \tau) = 0$.

Reactant fate and transport:

$$Y\phi \left(1 - \frac{1}{R}\right)\frac{\partial \Gamma}{\partial \tau} = \frac{\partial}{\partial \xi}\left(-\psi\left(\Gamma + \frac{1}{R-1}\right) + \beta_L \ell \left[\frac{\psi}{\phi}\right]\frac{\partial \Gamma}{\partial \xi}\right) - g_s(\phi)\Gamma \quad 0 \le \xi \le \ell, \tag{24}$$

with $\Gamma(\xi, 0) = 0$, $\Gamma(0, \tau) = 1$, and $\partial\Gamma/\partial\xi(\ell, \tau) = 0$.

3.2 Simplified Dimensionless Model

The values of the reactant supersaturation and yield are important in understanding the behavior of both the flow and the reactive transport equations. A large value of R will ensure the efficiency of the operation by providing ample supply of reactants. Here, our expectation is that $R > 10$, which is discussed further in the Supplementary Information. In terms of determining the yield, we note that the molar volume of the mineral precipitate is well constrained and will have a value of $O(10^{-5})$ [Parkhurst and Appelo, 2013]. The value of the initial concentration can be determined from the given injection condition. The field value reported from CarbFix 1 is 840 [mol/m^3] which would provide a value of the yield Y on the order of 0.01 [Snæbjörnsdóttir et al., 2018, 2020]. However, our model uses the *in-situ* concentration at the start of the precipitation, which we expect may be reduced from the injection value. Thus, it is reasonable to project that model values of Y will be less than 0.01. In the Supporting Information we further explore the possible value ranges for the parameters and terms in our dimensionless model.

Based on our understanding of the expected size of the yield, $Y < 0.01$, and initial supersaturation ratio, $R > 10$, we can, using the data values in our SI, make some simplifications of the governing dimensionless equations for flow and transport. We start this simplification by noting that:

1. In our current governing equations, the parameters $(1 - \rho_r)$, $g_s(\phi)$, and $(1 - 1/R)$ are all order 1.

2. Expected field values for the porosity and dispersion coefficient are $\phi \sim 0.1$ and $\beta_L \sim 0.1$ respectively, and are discussed in the supplementary information.

3. Values of the dimensionless domain length are $\ell < 10$; this is confirmed in subsequent analysis.

4. A representative dimensionless discharge is $\psi \sim \frac{1}{\ell}$, which, based on the expected domain length above, will take values between 0.1 and 1.

5. The dimensionless concentration is bounded in $0 < \Gamma \le 1$, with, due to its decreasing value with increasing ξ, an average domain value noticeably less than order 1.

8

In the light of this information, we can conclude that the left-hand side of (23) will take a value of order 10^{-2} or less, suggesting that it is reasonable to approximate the dimensionless discharge as divergence free. Further, with reference to eq.(24), we see that the ratios of the advection to transient terms $\left(\frac{1}{\ell Y \phi}\right)$ and dispersion to transient terms $\left(\frac{\beta_L \ell}{\phi^2 Y}\right)$ will be order 100 or larger. These imply that it is reasonable to neglect the transient term on the left-hand side of eq.(24). Assuming a divergence-free discharge and dropping the transient term in the transport equations, we arrive at a simplified dimensionless model for carbon mineralization:

Porosity:

$$\frac{\partial \phi}{\partial \tau} = -g_s(\phi)\Gamma \tag{25}$$

with $\phi(\xi, 0) = \phi_i$—identical to eq.(22).

Flow:

$$\frac{\partial}{\partial \xi}\left(g_k(\phi)\frac{\partial \eta}{\partial \xi}\right) = -\frac{\partial \psi}{\partial \xi} = 0 \tag{26}$$

with $\eta(0, \tau) = 1$ and $\eta(\ell, \tau) = 0$.

Reactant fate and transport:

$$-\psi\frac{\partial \Gamma}{\partial \xi} + \beta_L \ell \psi \frac{\partial}{\partial \xi}\left(\frac{1}{\phi}\frac{\partial \Gamma}{\partial \xi}\right) - g_s(\phi)\Gamma = 0 \tag{27}$$

with $\Gamma(0, \tau) = 1$, $\Gamma(\xi, \tau) = 0$, $(\partial \Gamma(\ell, \tau)/\partial \xi) = 0$, and includes the assumption of divergence-free flow.

Dropping terms that include the yield effectively states the rate of change of porosity is slow enough that its effect on the flow and transport can be neglected. We recognize that dropping these terms may result in some loss of accuracy, in particular when the yield is close to its upper limit of 0.01. However, in the context of our objective here, i.e., identification of the governing length and time scales of mineralization, assuming a divergence-free discharge and dropping the transient term in eq. (24) are both reasonable approximations. The key advantage of this step is that after providing appropriate constitutive models for hydraulic conductivity and specific surface area, we only need to specify the initial porosity ϕ_i and dimensionless longitudinal dispersivity β_L—aquifer intrinsic properties—to resolve the model.

4 Length and Time Scales for Carbon Mineralization Processes

4.1 Process Length

The simplified and dimensionless models for transport and flow are pseudo-steady state, changing only with the slowly changing porosity field. The implication is that, at given time τ, if we know the current porosity and surface area profiles, we can solve the steady-state equation given in eq. (27) to determine the current concentration profile $\Gamma(\xi, \tau)$. With this in hand, we can approximate an effective length $\ell_m(\tau)$ over which mineralization is occurring by locating the position where $\Gamma(\xi, \tau) = \Gamma_{ex}$, where Γ_{ex} is a small value (e.g., 0.01) that indicates a close to complete depletion of the reactant. We should expect that the point $\ell_m(\tau)$ will migrate backwards in time as the flow slows due to the decrease in porosity. Thus, the furthest extent that reactants will reach, defined as the *process length* ℓ_p, can be determined by solving eq. (27) for the initial $\Gamma(\xi, 0)$ profile. Following some rearrangement, this reduces to solving the ODE

$$\frac{d^2\Gamma}{d\xi^2} - \left[\frac{\phi_i}{\beta_L \ell_p}\right]\frac{d\Gamma}{d\xi} - \left[\frac{\phi_i}{\beta_L}\right]\Gamma = 0, \quad 0 \leq \xi \leq \ell_p, \quad \Gamma(0) = 1, \quad (d\Gamma(\ell_p)/d\xi) = 0; \tag{28}$$

note we are assuming the domain is at the process length ℓ_p and have imposed the initial time values for the constant porosity ϕ_i, $g_s(\phi) = 1$, and discharge $\psi_i = 1/\ell_p$. Equation (28) is a homogenous ODE with

9

constant coefficients. Since, by design $\Gamma(\ell_p, 0) = \Gamma_{ex}$ is small, we can arrive at an accurate approximate solution by replacing the zero gradient condition at $\xi = \ell_p$ with the condition $\Gamma(\xi, \tau) \to 0$ as $\xi \to \infty$, giving

$$\Gamma(\xi) = \exp(-a\xi); \qquad a = \frac{1}{2}\left(\sqrt{\left[\frac{\phi_i}{\beta_L \ell_p}\right]^2 + 4\left[\frac{\phi_i}{\beta_L}\right]} - \left[\frac{\phi_i}{\beta_L \ell_p}\right]\right). \tag{29}$$

This solution allows us to form the following relationship for the process length

$$a\ell_p = |\ln(\Gamma_{ex})|, \tag{30}$$

leaving the possibility open to provide alternative settings for the mineralization threshold concentration Γ_{ex}. Between the expression for the constant a in eq. (29) and the relationship in eq. (30), we can explicitly solve for the process length

$$\ell_p = \sqrt{|\ln(\Gamma_{ex})| + |\ln(\Gamma_{ex})|^2 \frac{\beta_L}{\phi_i}} \tag{31}$$

The value of ℓ_p obtained from the relationship in eq. (31) provides an optimum process length scale for a mineralization operation. If the extent of the field is much longer, then CO_2 will escape the system without mineralizing. In the opposite case, the domain will not be efficiently used. For $0.001 < \Gamma_{ex} < 0.1$, $0.1 < \phi_i < 0.3$, and $0 < \beta_L < 0.1$, we can find the range of l_p values as

$$2.1 \, (\Gamma_{ex} = 0.1, \phi, \beta_L = 0) < l_p < 7.4 \, (\Gamma_{ex} = 0.001, \phi_i = 0.1, \beta_L = 0.1), \tag{32}$$

which confirms $\ell < 10$. Values from this range can readily be converted to a dimensional length scale through eq. (21) giving

$$L_p = \ell_p \sqrt{\frac{K_i \Delta h}{k}} \tag{33}$$

4.2   Process Time to Shutoff

In addition to a characteristic length scale, we are also interested in determining a relevant timescale for shutoff, which indicates the operation timescale. On noting that complete precipitation-induced clogging of the pores will first occur at $x = 0$, where the reactant concentration is always at its highest value of $\Gamma = 1$, we can evaluate a shutoff time on direct solution of eq. (25). Using our generic specific surface area function in eq. (15), the porosity change equation at the entrance can be written as

$$\frac{\partial \phi}{\partial \tau} = -\frac{(1 - \phi)^m}{(1 - \phi_i)^m}, \quad 0 \leq m \leq 1, \tag{34}$$

with $\phi(\xi, 0) = \phi_i$. Defining complete shutoff to occur when we reach zero porosity at the entrance, i.e., $\phi(\xi = 0, \tau) = 0$, this equation is readily solved for the shutoff time using separation of variables. On recognizing that the shutoff time decreases monotonically with increasing values of m, we can consider bounding end member solutions of $m = 0$ or $m = 1$. In the former, the inlet porosity changes at a constant rate giving $\tau_{m=0} = \phi_i - \phi$. For the latter, $\tau_{m=1} = log\left(\frac{1-\phi_i}{1-\phi}\right)(\phi_i - 1)$. Solving each expression for the time when $\phi = 0$ gives

$$\tau_{m=0} = \phi_i, \quad \tau_{m=1} = (\phi_i - 1)\log(1 - \phi_i), \quad \tau_{m=0} > \tau_{m=1} \tag{35}$$

These two predictions are not much different. When $\phi_i = 0.1$, the linear case time is 0.0948, while the constant case time is 0.1. Since it provides an upper bound on the dimensionless time to shutoff, we propose adopting $\tau_{m=0} = \phi_i$ as the dimensionless process time scale. Substituting into the time scaling from the non-dimensionalization [eq. (21)], we obtain

$$t_{\text{off}} = \frac{\phi_i}{Yk}\left(\frac{R}{R - 1}\right) \approx \frac{\phi_i}{\nu_S C_0 k} \tag{36}$$

where we have used the facts that $R > 10$ and $Y = \nu_S C_0$.

4.3 Relevant Dimensionless Groups for Carbon Mineralization

We can also write out the field length scale in terms of the appropriate Damköhler numbers, which give the effective scales of reaction and transport relevant to a mineralization operation. Combining and rearranging eq.(31) and eq.(33) gives

$$L_p = \sqrt{|\ln(\Gamma_{ex})| + |\ln(\Gamma_{ex})|^2 \frac{\beta_L}{\phi_i}} \sqrt{\frac{K_i \Delta h}{k}}. \tag{37}$$

On noting that, at the initial time, $t = 0$, the dispersion can be parameterized as

$$D_i = \beta_L L_p \frac{q}{\phi_i} = \beta_L L_p \frac{K_i \Delta h}{L_p} \frac{1}{\phi_i} = \beta_L \frac{K_i \Delta h}{\phi_i}, \tag{38}$$

it follows from eq. (37) that

$$L_p = \Delta h \sqrt{\frac{|\ln(\Gamma_{ex})|}{\mathrm{Da_I}} + \frac{|\ln(\Gamma_{ex})|^2}{\mathrm{Da_{II}}}} \tag{39}$$

where

$$\mathrm{Da_I} = \frac{k \Delta h}{K_i} \tag{40}$$

is the first Damköhler number, expressing the ratio of reaction rate to advective transport rate, and

$$\mathrm{Da_{II}} = \frac{k \Delta h^2}{D_i} = \frac{k \Delta h \phi_i}{\beta_L K_i} \tag{41}$$

is the second Damköhler number, expressing the ratio of reaction rate to dispersive transport rate.

Thus, if we can determine the Damköhler numbers for a given field condition and specify the extent of mineralization required—i.e., setting the exit value of Γ_{ex}—we can obtain an estimate of the required process length. This scaling also indicates the main controls on the process length are both the intrinsic characteristics of the aquifers, K_i, ϕ_i, β_L, and k, as well as externally controlled parameters of the operation, Γ_{ex} and Δh. Likewise, our expression for shutoff times [eq. (36)] shows that the main extrinsic parameter setting shutoff is the injected reactant concentration, C_0, while the other parameters (ν_s, ϕ_i, k) are primarily controlled by the aquifer conditions. In this consideration, it is important to note that the value of C_0 is not necessarily the concentration injected at the wellhead because of aquifer geochemistry and mixing of injected waters with the ambient formation waters [Morse et al., 2007, Clark et al., 2020, Gysi and Stefánsson, 2011, Snæbjörnsdóttir et al., 2018]. These factors will cause the concentration of reactants when precipitation initiates to vary from the injected values.

5 Practical Applications of the Scaling Analysis

5.1 Estimates for parameter field values

Calculation of L_p and t_{off} requires estimation or determination of a few relevant field parameters beyond the parameters already discussed (i.e. Y, Γ_{ex}, etc.), specifically Δh, K_i, β_L, ϕ_i, and k. Here, we discuss some reasonable values of these parameters as an example of how these time and length scales can be used in field settings.

The constant head gradient: This is effectively set by the operator and is dependent on the pumps used as well as the formation characteristics. In our calculations here, we will use a fixed value of $\Delta h = 100$ m.

The dispersion coefficient: The value of β_L is ultimately defined by structure of the formation of itself, but can be characterized with field-testing of the target formation with passive tracer tests. Here, we consider $0 < \beta_L < 0.1$. This range is further discussed in the supplementary information.

The initial hydraulic conductivity: Conductivities can vary widely depending on the host rock (i.e. basalt) as well as the properties of the injected fluid after it has mixed with the formation water because of changing

temperature, CO_2 concentrations, etc. In many sites, the presence of fractures will further alter the effective conductivity and relative times of transport, or result in multiple domains with dramatically different conductivities [Viswanathan et al., 2022]. Based on reported permeability ranges for vesicular basalts and with water flow, we consider a range of $10^{-7} < K < 10^{-3}$ [m/s] [Saar and Manga, 1999, Clark et al., 2020, Snæbjörnsdóttir et al., 2020]. While this is a large range, this can be readily constrained through appropriate aquifer characterization.

The initial porosity: In the aquifers targeted for mineralization, one can expect a range of possible porosities, and the initial porosity for a given aquifer can be characterized as a part of site selection. Characterization of the target formation may necessarily suggest the use of functions $g_k(\phi)$ and $g_s(\phi)$ that are more appropriate to the specific site. The porosity is additionally necessary to understand beyond its impact on conductivity since it sets the maximum space where mineralization can occur and controls shutoff. Here, we consider $0.1 < \phi_i < 0.3$. This range is also briefly discussed in the supplementary information.

The first-order reaction rate constant: This term has the most uncertainty to it because of uncertainty in the underlying parameters, C_{eq}, k^*, and S_i, the equilibrium reactant concentration, geochemical reaction rate constant, and initial reactive surface area, respectively. The value of C_{eq} in the aquifer is a function of the precipitation reaction conditions and is discussed further in the supplementary information. While k^* can be determined from *ex-situ* experiments for a single mineral, it is well established that hydrodynamic conditions, mixing, and other dissolved solutes will influence the value of this relevant to *in-situ* conditions [Lasaga, 1995, 1997, Arvidson et al., 2003, Lin and Singer, 2005, Morse et al., 2007, Plummer et al., 1979, 1978, Kang et al., 2019]. These factors also do not consider the variable kinetics of the different metal carbonates that may form. Similarly, the value of S_i represents a continuing point of contention for modeling these reactions. Putting aside uncertainties resulting from mineralogical heterogeneity in a target aquifer, there even remain questions whether reactive surface areas should be derived from the geometry of the mineral surface, BET surface area measurements, or some other related parameter, which creates significant variability [Anovitz et al., 2022, Awolayo et al., 2022, Gouze et al., 2003, Gouze and Luquot, 2011, Morse et al., 2007, Helgeson et al., 1984, Noiriel et al., 2009]. The combination of these uncertainties result in k being very difficult to constrain *a priori*, but a representative range may be $10^{-8} < k < 10^{-3}$ [1/s].

So to summarize, to our best estimates, we consider the following possible field parameter values and ranges

$$
\begin{aligned}
Y &< 0.01 \\
0.001 < &\Gamma_{ex} < 0.01 \\
0 < &\beta_L < 0.1 \\
&\Delta h = 100 \text{ [m]} \\
0.1 < &\phi < 0.3 \\
10^{-7} < &K_i < 10^{-3} \text{ [m/s]} \\
10^{-8} < &k < 10^{-3} \text{ [1/s]}
\end{aligned}
\tag{42}
$$

5.2 Back calculation of reaction rate

The most striking feature of our estimates for field parameters in eq.(42) is the orders of magnitude range in the estimates for the reaction rate k and initial conductivity K_i. We saw above that eq. (31) predicts dimensionless process length to be within the relatively constrained values of 2 to 7. When we use these values along with our estimated range of field values in eq.(42) with eq.(37), the resulting dimensional penetration length falls within the range of

$$
20 \text{ cm} < L_p < 20 \text{ km};
\tag{43}
$$

this range captures what we might expect in the field, but its end values may not be feasible given current reports from mineralization efforts [Clark et al., 2020, Snæbjörnsdóttir et al., 2020, White et al., 2020].

The wide range in predicted field length scales is strongly controlled by the range of reaction rate constants and hydraulic conductivities, which are some of the principle unknowns in any carbonization operation.

Hydraulic conductivity can be constrained by careful aquifer characterization, but the *in-situ* value of k is more challenging to characterize. By contrast, the process length is obviously a known and the relative concentration at the exit well Γ_{ex}, can be readily measured. Thus, there is an opportunity to use our scaling in an 'inverse' sense to obtain an estimate of the 'effective' *in-situ* rate constant. This is accomplished by rewriting eq. (31) as

$$k = \frac{\ell_p^2 K_i \Delta h}{L_p^2},\tag{44}$$

which only requires an estimation of the length over which precipitation is occurring (defining both L_p and ℓ_p), in addition to the hydraulic parameters of the aquifer that are generally easier to estimate than k. For example, the CarbFix 1 injection had an approximate well separation of 125 m between the injection well and monitoring well where significant carbon removal had been observed [Snæbjörnsdóttir et al., 2018, 2017]. They also characterized the horizontal permeability to be 3×10^{-13} m^2, which, for water, gives a hydraulic conductivity around 3×10^{-6} [m/s]. Given the fact some dissolution occurred in that system, a reasonable range of L_p is 25 to 100 m. When used with the other parameters values in eq. (42) and eq. (32) this reduces the possible range on the reaction rate by almost 3 orders of magnitude

$$1 \times 10^{-7} < k < 2 \times 10^{-5} [1/\text{s}].$$

The point here is that with a given operating condition and the knowledge of hydraulic conductivity in the domain, this proposed scaling can be used to impose significant constraints on the effective first-order reaction rate constant.

5.3 Shut-off time

With a better constrained estimate of the effective reaction rate, we can use eq.(36) to improve the bounds on the time for shutoff. Presuming $\phi_i = 0.1$, $Y = 0.001$, and using the estimated values of k in eq.(5.2), the dimensional shutoff time falls in the range

$$50 \text{ days} < t_{\text{off}} < 30 \text{ years}$$

Returning to information from the CarbFix 1 site, we note that injection ran for approximately 90 days with no reported signs of clogging due to stored carbon [Snæbjörnsdóttir et al., 2020], suggesting that our analysis provides a meaningful time range. To some degree, for a given application, the shutoff time could be adjusted by decreasing or, if possible, increasing the supersaturation value, R, in the injected fluids.

6 Conclusions

By considering a simple model of mineral precipitation in a 1D porous media, we have developed a first-order model which represents the key processes relevant to carbon mineralization. By considering a dimensional analysis of this model, we have further identified the key length and time scales of the operation. These are specifically, the length of the domain where mineralization occurs,

$$L_p = \sqrt{|\ln(\Gamma_{ex})| + |\ln(\Gamma_{ex})|^2 \frac{\beta_L}{\phi_i}} \sqrt{\frac{K_i \Delta h}{k}}$$

and the time when clogging shuts off fluid flow,

$$t_{\text{off}} = \frac{\phi_i}{\nu_S C_0 k},$$

both of which depend on intrinsic aquifer properties and the operational parameters of the mineralization operation. These scales are necessary first steps to evaluate the total capacity of an aquifer and the time needed to realize that capacity. The scalings provide not only a sense for the required sizes and operation times of a mineralization project, but we have also shown that they can be used to place tighter constraints on the effective first-order reaction rate constant

$$k = \frac{\ell_p^2 K_i \Delta h}{L_p^2},$$

a vital, but poorly constrained parameter. Finally, the scales identified also confirm the critical characteristics that make for ideal mineralization: sufficient aquifer conductivity to allow injected CO_2 to access the target formation, moderate reactivity such that mineralization occurs quickly without rapid clogging, and sufficient pore space such that meaningful amounts of carbon can be stored. In light of those aquifer characteristics, the scalings suggest parameters that can be controlled (e.g., injection head and reactant concentrations) to engineer a desired domain size (length) and process time for a mineralization operation. Altogether, this study provides a powerful tool for understanding and optimizing *in-situ* carbon mineralization.

Open Research Section

The main data in this paper is developed from theoretical considerations, and no additional data is required to interpret or reproduce the work here. Any cited data, including parameter values derived in the supplementary information, was derived solely from the referenced values from the literature.

Acknowledgements

References

Lawrence M. Anovitz, Lauren E. Beckingham, Julia M. Sheets, and David R. Cole. A Quantitative Approach to the Analysis of Reactive Mineralogy and Surface Area. *ACS Earth and Space Chemistry*, 6(2):272–287, February 2022. doi: 10.1021/acsearthspacechem.1c00198.

Rolf S. Arvidson, Inci Evren Ertan, James E. Amonette, and Andreas Luttge. Variation in calcite dissolution rates:: A fundamental problem? *Geochimica et Cosmochimica Acta*, 67(9):1623–1634, May 2003. ISSN 0016-7037. doi: 10.1016/S0016-7037(02)01177-8.

Adedapo N. Awolayo, Christiaan T. Laureijs, John Byng, Andrew J. Luhmann, Rachel Lauer, and Benjamin M. Tutolo. Mineral surface area accessibility and sensitivity constraints on carbon mineralization in basaltic aquifers. *Geochimica et Cosmochimica Acta*, 334:293–315, October 2022. ISSN 0016-7037. doi: 10.1016/j.gca.2022.08.011.

Jacob Bear. *Dynamics of Fluids in Porous Media*. Dover, 1972. ISBN 978-0-486-65675-5.

Ben Callow, Ismael Falcon-Suarez, Sharif Ahmed, and Juerg Matter. Assessing the carbon sequestration potential of basalt using X-ray micro-CT and rock mechanics. *International Journal of Greenhouse Gas Control*, 70:146–156, March 2018. ISSN 1750-5836. doi: 10.1016/j.ijggc.2017.12.008.

P. C. Carman. Fluid flow through granular beds. *Chemical Engineering Research and Design*, 75:S32–S48, December 1997. ISSN 0263-8762. doi: 10.1016/S0263-8762(97)80003-2.

Deirdre E. Clark, Eric H. Oelkers, Ingvi Gunnarsson, Bergur Sigfússon, Sandra Ó. Snæbjörnsdóttir, Edda S. Aradóttir, and Sigurður R. Gíslason. CarbFix2: CO2 and H2S mineralization during 3.5 years of continuous injection into basaltic rocks at more than 250 ºC. *Geochimica et Cosmochimica Acta*, 279:45–66, June 2020. ISSN 0016-7037. doi: 10.1016/j.gca.2020.03.039.

Lynn W. Gelhar, Claire Welty, and Kenneth R. Rehfeldt. A critical review of data on field-scale dispersion in aquifers. *Water Resources Research*, 28(7):1955–1974, 1992. ISSN 1944-7973. doi: 10.1029/92WR00607.

Philippe Gouze and Linda Luquot. X-ray microtomography characterization of porosity, permeability and reactive surface changes during dissolution. *Journal of Contaminant Hydrology*, 120-121:45–55, 2011. ISSN 0169-7722. doi: 10.1016/j.jconhyd.2010.07.004.

Philippe Gouze, Catherine Noiriel, Céline Bruderer, Didier Loggia, and Richard Leprovost. X-ray tomography characterization of fracture surfaces during dissolution. *Geophysical Research Letters*, 30(5), 2003. ISSN 1944-8007. doi: 10.1029/2002GL016755.

Alexander P. Gysi and Andri Stefánsson. CO2-water-basalt interaction. Numerical simulation of low temperature CO2 sequestration into basalts. *Geochimica et Cosmochimica Acta*, 75(17):4728–4751, September 2011. ISSN 0016-7037. doi: 10.1016/j.gca.2011.05.037.

Harold C. Helgeson, William M. Murphy, and Per Aagaard. Thermodynamic and kinetic constraints on reaction rates among minerals and aqueous solutions. II. Rate constants, effective surface area, and the hydrolysis of feldspar. *Geochimica et Cosmochimica Acta*, 48(12):2405–2432, December 1984. ISSN 0016-7037. doi: 10.1016/0016-7037(84)90294-1.

Peter K. Kang, Etienne Bresciani, Seongnam An, and Seunghak Lee. Potential impact of pore-scale incomplete mixing on biodegradation in aquifers: From batch experiment to field-scale modeling. *Advances in Water Resources*, 123:1–11, January 2019. ISSN 0309-1708. doi: 10.1016/j.advwatres.2018.10.026.

Peter B. Kelemen, Noah McQueen, Jennifer Wilcox, Phil Renforth, Greg Dipple, and Amelia Paukert Vankeuren. Engineered carbon mineralization in ultramafic rocks for CO2 removal from air: Review and new insights. *Chemical Geology*, 550:119628, September 2020. ISSN 00092541. doi: 10.1016/j.chemgeo.2020.119628.

J. Kozeny. Ueber kapillare Leitung des Wassers im Boden. *Sitzungsberichte Akademie der Wissenschaften in Wien*, 126(2a):271–306, April 1927.

Antonio C. Lasaga. Fundamental approaches in describing mineral dissolution and precipitation rates. *Reviews in Mineralogy and Geochemistry*, 31(1):23–86, January 1995. ISSN 1529-6466.

Antonio C. Lasaga. *Kinetic Theory in the Earth Sciences*. Princeton University Press, 1 edition, 1997.

Yi-Pin Lin and Philip C. Singer. Effects of seed material and solution composition on calcite precipitation. *Geochimica et Cosmochimica Acta*, 69(18):4495–4504, September 2005. ISSN 0016-7037. doi: 10.1016/j.gca.2005.06.002.

Juerg M. Matter, Martin Stute, Sandra Ó Snæbjörnsdóttir, Eric H. Oelkers, Sigurdur R. Gislason, Edda S. Aradottir, Bergur Sigfusson, Ingvi Gunnarsson, Holmfridur Sigurdardottir, Einar Gunnlaugsson, Gudni Axelsson, Helgi A. Alfredsson, Domenik Wolff-Boenisch, Kiflom Mesfin, Diana Fernandez de la Reguera Taya, Jennifer Hall, Knud Dideriksen, and Wallace S. Broecker. Rapid carbon mineralization for permanent disposal of anthropogenic carbon dioxide emissions. *Science*, 352(6291):1312–1314, June 2016. doi: 10.1126/science.aad8132.

John W. Morse, Rolf S. Arvidson, and Andreas Lüttge. Calcium Carbonate Formation and Dissolution. *Chemical Reviews*, 107(2):342–381, February 2007. ISSN 0009-2665. doi: 10.1021/cr050358j.

G. H Nancollas and M. M Reddy. The crystallization of calcium carbonate. II. Calcite growth mechanism. *Journal of Colloid and Interface Science*, 37(4):824–830, December 1971. ISSN 0021-9797. doi: 10.1016/0021-9797(71)90363-8.

Catherine Noiriel, Linda Luquot, Benoît Madé, Louis Raimbault, Philippe Gouze, and Jan van der Lee. Changes in reactive surface area during limestone dissolution: An experimental and modelling study. *Chemical Geology*, 265(1):160–170, July 2009. ISSN 0009-2541. doi: 10.1016/j.chemgeo.2009.01.032.

D.L. Parkhurst and C.A.J. Appelo. Description of Input and Examples for PHREEQC Version 3 — A Computer Program for Speciation , Batch-Reaction , One-Dimensional Transport , and Inverse Geochemical Calculations. In *book 6, ch. A43*, U.S. Geological Survey Techniques and Methods, page 497. United States Geological Survey, 2013. Available only at https://pubs.usgs.gov/tm/06/a43/.

L. N. Plummer, T. M. L. Wigley, and D. L. Parkhurst. The kinetics of calcite dissolution in CO 2 -water systems at 5 degrees to 60 degrees C and 0.0 to 1.0 atm CO 2. *American Journal of Science*, 278(2): 179–216, February 1978. ISSN 0002-9599, 1945-452X. doi: 10.2475/ajs.278.2.179.

L. N. Plummer, D. L. Parkhurst, and T. M. L. Wigley. Critical Review of the Kinetics of Calcite Dissolution and Precipitation. In Everett A. Jenne, editor, *Chemical Modeling in Aqueous Systems*, volume 93, pages 537–573. AMERICAN CHEMICAL SOCIETY, WASHINGTON, D. C., March 1979. ISBN 978-0-8412-0479-9 978-0-8412-0616-8. doi: 10.1021/bk-1979-0093.ch025.

Ian M. Power, Anna L. Harrison, Gregory M. Dipple, Sasha Wilson, Peter B. Kelemen, Michael Hitch, and Gordon Southam. Carbon Mineralization: From Natural Analogues to Engineered Systems. *Reviews in Mineralogy and Geochemistry*, 77(1):305–360, January 2013. ISSN 1529-6466. doi: 10.2138/rmg.2013.77.9.

M. M. Reddy and G. H. Nancollas. The crystallization of calcium carbonate: IV. The effect of magnesium, strontium and sulfate ions. *Journal of Crystal Growth*, 35(1):33–38, August 1976. ISSN 0022-0248. doi: 10.1016/0022-0248(76)90240-2.

Michael M Reddy and George H Nancollas. The crystallization of calcium carbonate: I. Isotopic exchange and kinetics. *Journal of Colloid and Interface Science*, 36(2):166–172, June 1971. ISSN 0021-9797. doi: 10.1016/0021-9797(71)90161-5.

Martin O. Saar and Michael Manga. Permeability-porosity relationship in vesicular basalts. *Geophysical Research Letters*, 26(1):111–114, 1999. ISSN 1944-8007. doi: 10.1029/1998GL900256.

Mollie S. Sabo and Lauren E. Beckingham. Porosity-Permeability Evolution During Simultaneous Mineral Dissolution and Precipitation. *Water Resources Research*, 57(6):e2020WR029072, 2021. ISSN 1944-7973. doi: 10.1029/2020WR029072.

Sandra Ó. Snæbjörnsdóttir, Eric H. Oelkers, Kiflom Mesfin, Edda Sif Aradóttir, Knud Dideriksen, Ingvi Gunnarsson, Einar Gunnlaugsson, Juerg M. Matter, Martin Stute, and Sigurdur R. Gislason. The chemistry and saturation states of subsurface fluids during the in situ mineralisation of CO2 and H2S at the CarbFix site in SW-Iceland. *International Journal of Greenhouse Gas Control*, 58:87–102, March 2017. ISSN 1750-5836. doi: 10.1016/j.ijggc.2017.01.007.

Sandra Ó. Snæbjörnsdóttir, Sigurdur R. Gislason, Iwona M. Galeczka, and Eric H. Oelkers. Reaction path modelling of in-situ mineralisation of CO2 at the CarbFix site at Hellisheidi, SW-Iceland. *Geochimica et Cosmochimica Acta*, 220:348–366, January 2018. ISSN 0016-7037. doi: 10.1016/j.gca.2017.09.053.

Sandra Ó. Snæbjörnsdóttir, Bergur Sigfússon, Chiara Marieni, David Goldberg, Sigurður R. Gislason, and Eric H. Oelkers. Carbon dioxide storage through mineral carbonation. *Nature Reviews Earth & Environment*, 1(2):90–102, February 2020. ISSN 2662-138X. doi: 10.1038/s43017-019-0011-8.

H. S. Viswanathan, J. Ajo-Franklin, J. T. Birkholzer, J. W. Carey, Y. Guglielmi, J. D. Hyman, S. Karra, L. J. Pyrak-Nolte, H. Rajaram, G. Srinivasan, and D. M. Tartakovsky. From Fluid Flow to Coupled Processes in Fractured Rock: Recent Advances and New Frontiers. *Reviews of Geophysics*, 60(1):e2021RG000744, 2022. ISSN 1944-9208. doi: 10.1029/2021RG000744.

Signe K. White, Frank A. Spane, H. Todd Schaef, Quin R. S. Miller, Mark D. White, Jake A. Horner, and B. Peter McGrail. Quantification of CO2 Mineralization at the Wallula Basalt Pilot Project. *Environmental Science & Technology*, 54(22):14609–14616, November 2020. ISSN 0013-936X. doi: 10.1021/acs.est.0c05142.